Received: 21 October 2016 | Revised: 28 March 2017 | Accepted: 29 May 2017

DOI: 10.1002/fld.4400

RESEARCH ARTICLE

WILEY

Constrained moving least-squares immersed boundary method for fluid-structure interaction analysis

Yegao Qu[1,2] | Romesh C. Batra[1]

[1] Department of Biomedical Engineering and Mechanics, Virginia Polytechnic Institute and State University, M/C 0219, Blacksburg, VA 24061, USA

[2] State Key Laboratory of Mechanical System and Vibration, Shanghai Jiao Tong University, Shanghai 200240, China

Correspondence
Romesh C. Batra, Department of Biomedical Engineering and Mechanics, Virginia Polytechnic Institute and State University, M/C 0219, Blacksburg, VA 24061, USA
Email: rbatra@vt.edu

Funding information
US Office of Naval Research, Grant/Award Number: N00014-16-1-2309

Summary

A numerical method is presented for the analysis of interactions of inviscid and compressible flows with arbitrarily shaped stationary or moving rigid solids. The fluid equations are solved on a fixed rectangular Cartesian grid by using a higher-order finite difference method based on the fifth-order WENO scheme. A constrained moving least-squares sharp interface method is proposed to enforce the Neumann-type boundary conditions on the fluid-solid interface by using a penalty term, while the Dirichlet boundary conditions are directly enforced. The solution of the fluid flow and the solid motion equations is advanced in time by staggerly using, respectively, the third-order Runge-Kutta and the implicit Newmark integration schemes. The stability and the robustness of the proposed method have been demonstrated by analyzing 5 challenging problems. For these problems, the numerical results have been found to agree well with their analytical and numerical solutions available in the literature. Effects of the support domain size and values assigned to the penalty parameter on the stability and the accuracy of the present method are also discussed.

KEYWORDS

compressible flow, constrained moving least-squares interpolation, fluid-structure interaction, immersed boundary method, shock

1 | INTRODUCTION

Interactions between compressible flows and complex-shaped solids are commonly encountered in many engineering applications. These interactions may encompass a variety of flow phenomena, including shock-wave reflection and diffraction, shock-shock, and shock-vortex interactions. The simulation of fluid-solid interactions (FSIs) involving flow discontinuities (e.g., shock waves) and irregularly shaped solids poses a formidable challenge to even the most advanced numerical methods and is currently a research topic in computational fluid dynamics.

During the last few decades, extensive attention has been paid to the development of accurate and efficient numerical methods to study the FSI problems involving complex stationary and moving boundaries. Traditionally, the body-fitted or unstructured grid methods[1,2] are used to analyze such problems. However, these methods require the generation of body-fitted fluid meshes, which is a cumbersome task for complicated solid boundaries. In addition, for time-evolving moving-boundary problems, the fluid mesh needs to be updated or re-meshed to accommodate the solid deformations or motion. The successive projection of the flow field solutions from the previous mesh to the new one is prone to errors. In recent years, immersed boundary methods[3] have become popular for simulations of FSIs involving solids with complex boundaries. The essence of these methods is that the fluid and the solid are modeled, respectively, in Eulerian and Lagrangian frames,

and equations governing the fluid flow are solved on a fixed grid, which conforms to that of the solid. This considerably simplifies the grid generation especially for FSI problems involving moving boundaries, where the need for regeneration of the fluid mesh is eliminated. In addition, because the fluid grid is typically structured, the application of an efficient Cartesian grid solver is straightforward. Although immersed boundary methods have many advantages, the treatment of boundary conditions on a fluid-solid interface is complicated.

A variety of methods have been developed to enforce boundary conditions on an immersed boundary. Based on the representation of a fluid-solid interface, the immersed boundary methods may be classified as either diffused or sharp interface methods.[3] In the diffused interface methods,[4-6] the fluid-solid interface is smeared by distributing singular forces over several grid nodes in the vicinity of the immersed boundary using special functions. A major issue with the diffused interface methods is that they require excessively fine grids near the immersed boundary to accurately resolve it. The sharp interface methods[7-10] strongly depend on the spatial discretization of the immersed boundary in which a solid boundary is precisely tracked. The advantage of the sharp interface methods is that for certain formulations, they allow for a "sharp" representation of the immersed boundary. By contrast, the diffused interface methods produce a "diffuse" boundary and the boundary conditions on the immersed boundary are not satisfied at its actual location but within a localized region around the boundary.[10]

A critical issue in a sharp interface immersed boundary method is the reconstruction of the solution at nodes nearest to the immersed interface via appropriate interpolation schemes using known values on the solid surface and the information from the interior of the flow.[11] The reconstruction determines both the global spatial accuracy of such methods and their adaptability to flow computations with arbitrarily complex immersed boundaries. The commonly used schemes for the reconstruction of flow values are the bilinear interpolation for 2-dimensional (2-D) problems[7] and the trilinear interpolation for 3-D problems.[9] However, when the interpolation point is very close to the boundary, it may become difficult to accurately find values of flow variables at the point. For example, in a 2-D problem, all 4 neighboring points required for the bilinear interpolation may not be in the fluid domain. In such cases, the information at the desired point can be found either by using a reduced-order interpolation scheme or by using boundary-intercepting points for the interpolation. The inverse distance weighting interpolation method has also been used to construct the fluid values in sharp interface immersed boundary methods.[7,11,12] This scheme is stable for reconstructing variables that smoothly vary without exhibiting a large maximum value. The accuracy of the above-mentioned methods is at most second order. It should be noted that the interpolation using higher-order polynomials is expected to be more accurate, but they often lead to numerical instabilities. Moreover, higher-order formulations require large interpolation stencils, which may intersect the immersed boundaries, and the determination of appropriate stencils for the interpolation may be difficult. A method is, therefore, needed that will enable higher-order boundary formulations while allowing for a high degree of flexibility with respect to the interpolation stencil. This can be achieved by using the moving least-squares (MLS) reconstruction scheme.[13,14] Seo and Mittal[15] applied an MLS method based on a high-order approximating polynomial to construct the flow values near the immersed boundaries. Their results showed that the convergence rate of the method is about 5 for very fine grids and about 3 for coarse grids. The key to the successful implementation of this method is to maintain the well posedness of the least-squares error problem.

The main objective of this study is to develop a robust numerical method for FSI analyses of inviscid and compressible flows with arbitrarily shaped stationary or moving rigid solids. A constrained MLS sharp interface method is proposed to enforce coupling conditions on the fluid-solid interface. The Neumann-type boundary conditions on the interface are imposed by incorporating a penalty term in the MLS formulation, whereas the Dirichlet boundary conditions are directly enforced. To estimate the robustness and the accuracy of the proposed constrained MLS method, simulation results for several test problems are presented and compared with their analytical/numerical solutions available in the literature.

The remainder of the paper is organized as follows. In Section 2, equations governing the fluid flow and the solid motion are described. Numerical methods, including the finite difference WENO scheme and the constrained MLS immersed boundary method, are presented in Section 3. Numerical results for 5 example problems are presented and discussed in Section 4 to demonstrate the accuracy and the robustness of the present method. Concluding remarks are given in Section 5.

2 | PROBLEM FORMULATION

Consider the problem of a rigid solid moving in a compressible fluid. The rigid body and the fluid, respectively, occupy finite domains Ω_s and Ω_f at time t having the common boundary, Γ_{sf}. Euler equations governing the 2-D flow in the x_1x_2 plane of an inviscid, homogeneous, and compressible fluid can be written as

$$\frac{\partial \mathbf{Q}}{\partial t} + \frac{\partial \mathbf{E}}{\partial x_1} + \frac{\partial \mathbf{F}}{\partial x_2} = 0, \tag{1}$$

where $\mathbf{Q}=[\rho,\rho u_1,\rho u_2,E]^{\mathrm{T}}$ is the vector of conserved variables; $\mathbf{E}=\left[\rho u_1,\rho u_1^2+p,\rho u_1 u_2,(E+p)u_1\right]^{\mathrm{T}}$ and $\mathbf{F}=\left[\rho u_2,\rho u_1 u_2,\rho u_2^2+p,(E+p)u_2\right]^{\mathrm{T}}$ are flux vectors in the x_1 and the x_2 directions, respectively; ρ is the fluid mass density; u_i $(i=1,2)$ is the velocity of the fluid in the x_i direction; p is the pressure; and E is the specific total energy. The effect of gravity is not considered. Equation (1) is supplemented with the following equation of state for an ideal gas

$$p=(\gamma-1)\left(E-\frac{1}{2}\rho u_k u_k\right), \tag{2}$$

where γ is the ratio of the 2 specific heats and is taken as 1.4 for air, and a repeated index implies summation over the range of the index.

Equations of motion for the rigid solid are written as

$$\frac{d\mathbf{X}_c}{dt}=\mathbf{U},\quad M\frac{d\mathbf{U}}{dt}=\mathbf{F}_s+\mathbf{F}_f, \tag{3}$$

$$\frac{d\Theta}{dt}=\omega,\quad J\frac{d\omega}{dt}=T_s+T_f\,, \tag{4}$$

where $\mathbf{X}_c$ is the translational displacement of the mass center of the solid, and Θ is the angular displacement between a reference line and a body-fixed line. $\mathbf{U}$ and ω are the translational velocity vector and the angular velocity of the solid about the x_3-axis, respectively. M and J are the mass and the moment of inertia of the body about the x_3-axis, respectively. $\mathbf{F}_s$ and T_s are the external force and the external torque about the x_3-axis acting about the x_3-axis on the solid that are not associated with the fluid motion. $\mathbf{F}_f$ and T_f are the net force and the net torque imparted by the fluid to the solid.

On the fluid-solid interface, the normal component of the fluid velocity must match that of the solid. That is,

$$\mathbf{u}(\mathbf{X}_\Gamma(t),t)\cdot\mathbf{n}=\mathbf{U}\cdot\mathbf{n}, \tag{5}$$

where $\mathbf{u}$ and $\mathbf{U}$, respectively, denote the velocity of the contacting fluid and the solid particles with the position vector $\mathbf{X}_\Gamma(t)$, and $\mathbf{n}$ is a unit vector normal to the fluid-solid interface.

The fluid force and the moment exerted on the rigid body are given by

$$\mathbf{F}_f=\int_{\Gamma_{sf}}(-p\mathbf{n})d\Gamma, \tag{6}$$

$$T_f=\int_{\Gamma_{sf}}\left(\mathbf{X}_\Gamma-\widehat{\mathbf{X}}_c\right)\times(-p\mathbf{n})d\Gamma, \tag{7}$$

where $\widehat{X}_c$ denotes the position vector of the center of mass of the solid. In order to complete the problem formulation, initial conditions and an additional boundary condition on $\mathbf{X}_\Gamma(t)$ are needed. The latter is listed as Equation (17) below and the former are prescribed for each problem studied.

3 | NUMERICAL METHODS

3.1 | Fluid field discretization

The governing equations of the fluid are discretized on a uniform Cartesian grid. The semi-discrete form of Equation 1 is written as

$$\frac{\partial\mathbf{Q}_{i,j}}{\partial t}+\frac{1}{\Delta x_1}\left(\mathbf{E}_{i+1/2,j}-\mathbf{E}_{i-1/2,j}\right)+\frac{1}{\Delta x_2}\left(\mathbf{F}_{i,j+1/2}-\mathbf{F}_{i,j-1/2}\right)=\mathbf{0}, \tag{8}$$

where $\mathbf{Q}_{i,j}$ is the vector of conserved variables at the (i,j)th grid node (i,j are the grid indices), Δx_1 and Δx_2 are the grid spacing, $\mathbf{E}_{i\pm1/2,j}$ are fluxes at the right and the left cell boundaries, and $\mathbf{F}_{i,j\pm1/2}$ are fluxes at the top and the bottom cell boundaries.

We split the flux vectors $\mathbf{E}_{i\pm1/2,j}$ and $\mathbf{F}_{i,j\pm1/2}$ into the sum of positive and negative components:

$$\mathbf{E}_{i\pm1/2,j}=\mathbf{E}^{+}_{i\pm1/2,j}+\mathbf{E}^{-}_{i\pm1/2,j},\quad \mathbf{F}_{i,j\pm1/2}=\mathbf{F}^{+}_{i,j\pm1/2}+\mathbf{F}^{-}_{i,j\pm1/2}\,. \tag{9}$$

The Lax-Friedrichs flux splitting method[16] is used to numerically calculate the fluxes $\mathbf{E}^{\pm}$ and $\mathbf{F}^{\pm}$:

$$\mathbf{E}^{\pm}=\frac{1}{2}(\mathbf{E}\pm\mathbf{R}|\mathbf{\Lambda}|\mathbf{L}\mathbf{Q}),\quad \mathbf{F}^{\pm}=\frac{1}{2}(\mathbf{F}\pm\mathbf{T}|\mathbf{\Psi}|\mathbf{S}\mathbf{Q})\,. \tag{10}$$

The calculation of $\mathbf{E}^{\pm}$ and $\mathbf{F}^{\pm}$ requires interpolated values of the fluxes $\mathbf{E}$, $\mathbf{F}$ and the conserved variable vector $\mathbf{Q}$ at the interfaces, which are determined by using the fifth-order WENO scheme.[17-19]

The basic idea underlying the WENO approach is to introduce a convex linear combination of low-order polynomial reconstructions that yields high-order resolution in smooth regions and keeps the essentially non-oscillatory property near discontinuities. Depending on the choice of the numerical scheme, the actual stencil coefficients and weights are different.[20] We describe the WENO scheme for a 1-D scalar problem, and the variable φ is used to represent either the variable or the flux. The WENO scheme computes numerical fluxes $\varphi^{\pm}_{i+1/2}$ at the cell interface $i+1/2$ through interpolated polynomials on a number of grid points per candidate stencil. The WENO reconstruction for $\varphi^{\pm}_{i+1/2}$ in the x_1 direction is[17]

$$\varphi^{+}_{i+1/2}=\sum_{k=0}^{K-1}\varpi_k\widehat{\varphi}^{k}_{i+1/2}, \tag{11}$$

where K is the number of candidate stencils, $\widehat{\varphi}^{k}_{i+1/2}$ is the interface variable/flux based on the kth candidate stencil, and ϖ_k is a non-linear weight coefficient. A $(2K-1)$th-order accurate numerical approximation can be obtained by choosing optimal upwind biased weight coefficients.

For the fifth-order WENO scheme, $K=3$, and $\widehat{\varphi}^{k}_{i+1/2}$ is given by

$$\widehat{\varphi}^{0}_{i+1/2}=\frac{2\varphi^{+}_{i}+5\varphi^{+}_{i+1}-\varphi^{+}_{i+2}}{6},\quad \widehat{\varphi}^{1}_{i+1/2}=\frac{-\varphi^{+}_{i-1}+5\varphi^{+}_{i}+2\varphi^{+}_{i+1}}{6},\quad \widehat{\varphi}^{2}_{i+1/2}=\frac{2\varphi^{+}_{i-2}-7\varphi^{+}_{i-1}+11\varphi^{+}_{i}}{6}. \tag{12}$$

The weight coefficient ϖ_k is defined by

$$\varpi_k=\frac{\alpha_k}{\sum_{l=0}^{2}\alpha_l},\quad \alpha_k=\frac{d_k}{(\varepsilon+\beta_k)^p}, \tag{13}$$

where d_0, d_1, and d_2 equal 0.3, 0.6, and 0.1, respectively. The exponent p is set equal to 2 to achieve fast convergence to zero in non-smooth flow regions, $\varepsilon=10^{-6}$ is a small parameter used to avoid the denominator becoming zero, and

$$\beta_0=\frac{13}{12}\left(\varphi_i-2\varphi_{i+1}+\varphi_{i+2}\right)^2+\frac{1}{4}\left(3\varphi_i-4\varphi_{i+1}+\varphi_{i+2}\right)^2, \tag{14}$$

$$\beta_1=\frac{13}{12}\left(\varphi_{i-1}-2\varphi_i+\varphi_{i+1}\right)^2+\frac{1}{4}\left(\varphi_{i-1}-\varphi_{i+1}\right)^2, \tag{15}$$

$$\beta_2=\frac{13}{12}(\varphi_{i-2}-2\varphi_{i-1}+\varphi_i)^2+\frac{1}{4}(\varphi_{i-2}-4\varphi_{i-1}+3\varphi_i)^2, \tag{16}$$

are the smoothness indicators.

For computing the numerical flux $\varphi^{-}_{i+1/2}$, the previously mentioned procedure is modified symmetrically with respect to $i+1/2$.

The third-order total variation diminishing Runge-Kutta scheme is used for the time integration of Equation 8.

3.2 | Sharp interface immersed boundary method

The fluid flow over a complex solid is found by solving Equation 1 on a fixed structured grid that is not necessarily aligned with the solid. We use the sharp interface immersed boundary method[10] to study the interaction of the fluid flow with arbitrarily shaped stationary or moving solids. Algorithmically, the sharp interface immersed boundary method involves 2 steps: (a) the grid node classification and (b) the reconstruction of the flow variables and imposition of appropriate boundary conditions in the immediate vicinity of the immersed body. At each time instant, all nodes on the Cartesian grid are divided into 2 groups for the given position and the geometry of the solid, namely, the fluid nodes and the solid nodes, depending on which side of the fluid/solid interface a node is located. A solid node immediately next to the fluid-solid interface is termed a "ghost point" (GP) (see Figure 1). A set of Lagrangian solid marker points is used to represent the surface of the solid, and these points are generated by using a piecewise linear spatial discretization scheme. A "normal probe" is extended from a GP to intersect with the immersed boundary (at a boundary point denoted as the "boundary intercept" [BI]). The probe is extended into the fluid to the "image point" (IP) such that the BI is midway between the image and the GPs. The fifth-order WENO scheme needs up to 3 GPs in each x_i direction. An efficient ray-tracing technique[21] is used to select these GPs. Referring the reader to O'Rourke[21] for details, we note that it involves casting a random half-infinite ray starting from the point under consideration and determining the points where it intersects the discretized edges of the solid boundary. If the number of points of intersections is odd, then the point closest to the starting point is located inside the solid, and identified as GP.

The procedure of a sharp interface immersed boundary method is to interpolate values of the fluid variables at the IPs in terms of those of the surrounding fluid nodes and then use these values and the fluid-solid boundary conditions to determine the corresponding values at the ghost nodes. Boundary conditions are imposed by prescribing the primitive variables at the GPs. Before giving details of the method, we describe the numerical boundary conditions on the fluid-solid interface. According to Equation 5, the normal velocity component u_n of the fluid particle equals the normal velocity U_n of the solid particle at the same location on the interface. The normal derivatives of the tangential velocity u_τ and of the mass density on the fluid-solid interface are assumed to be zero, i.e., $\partial u_\tau/\partial n = 0$ and $\partial \rho/\partial n = 0$. A Neumann-type boundary condition for the pressure is obtained from the momentum equation by projecting the pressure gradient onto the surface-normal direction[22]:

$$-\nabla p|_{BI}\cdot\mathbf{n} = -\left.\frac{\partial p}{\partial n}\right|_{BI} = -\left.\left(\frac{\rho u_\tau^2}{R}\right)\right|_{BI} + \left.\left(\rho\frac{D\mathbf{u}}{Dt}\right)\right|_{BI}\cdot\mathbf{n}, \tag{17}$$

where R is the signed local radius of the wall curvature of $\mathbf{X}_\Gamma(t)$ taken as positive (negative) if the center of curvature is on the side of the solid (fluid) body. The quantity, $\partial\mathbf{u}/\partial t$, on the right-hand side of Equation (17) is the acceleration of the material

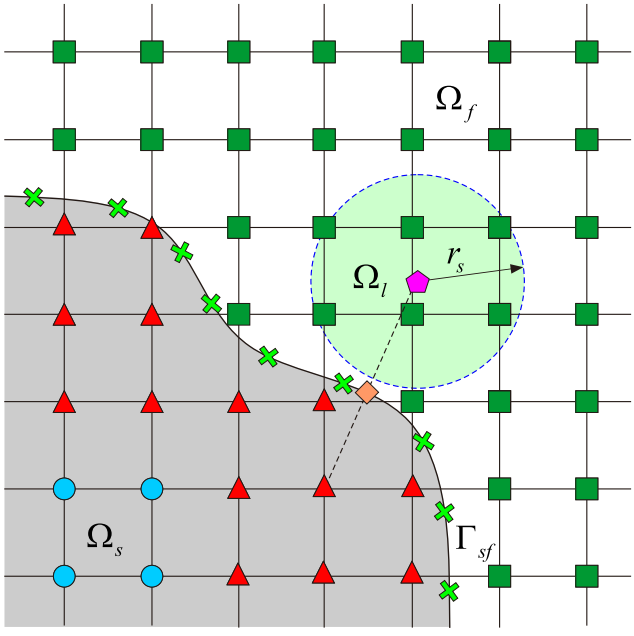

FIGURE 1 Definitions of various points in immersed boundary method: ■, fluid node; ●, solid node; ✕, solid marker; ◆, boundary intercept (BI); ⬟, image point or node; ▲, ghost point or node [Colour figure can be viewed at wileyonlinelibrary.com]

node on the interface. For a stationary or steadily moving rigid solid, $\partial \mathbf{u}/\partial t$ is approximated as zero, and the boundary condition for the pressure becomes $\partial p/\partial n = \rho u_\tau^2/R$.

A constrained MLS method is proposed to approximate the value of a generic variable φ at an IP $\bar{\mathbf{x}}$ in a local support domain Ω_l (see Figure 1). A local rectangular Cartesian coordinate system $(\varsigma_1, \varsigma_2)$ is introduced at the IP. Thus, for an arbitrary point $\mathbf{x}(\in\Omega_l)$, $\boldsymbol{\varsigma} = \mathbf{x}-\bar{\mathbf{x}}$. In the local coordinate system, the distribution of $\varphi(\boldsymbol{\varsigma})$ in Ω_l, over a number of fluid nodes $\{\boldsymbol{\varsigma}_i\}$, $i=1,2,\cdots,N$, is represented in terms of the m basis functions $\boldsymbol{\psi}^{\mathrm{T}}(\boldsymbol{\varsigma})=[\psi_1(\boldsymbol{\varsigma}),\psi_2(\boldsymbol{\varsigma}),\cdots,\psi_m(\boldsymbol{\varsigma})]$:

$$\varphi^h(\boldsymbol{\varsigma}) = \sum_{i=1}^{m}\psi_i(\boldsymbol{\varsigma})\eta_i(\boldsymbol{\varsigma}) = \boldsymbol{\psi}^{\mathrm{T}}(\boldsymbol{\varsigma})\boldsymbol{\eta}(\boldsymbol{\varsigma}), \quad \forall\boldsymbol{\varsigma}\in\Omega_l\,, \tag{18}$$

where $\varphi^h(\boldsymbol{\varsigma})$ is the approximant of $\varphi(\boldsymbol{\varsigma})$, and $\boldsymbol{\eta}(\boldsymbol{\varsigma})$ is a coefficient vector defined as $\boldsymbol{\eta}(\boldsymbol{\varsigma})=[\eta_1(\boldsymbol{\varsigma}),\eta_2(\boldsymbol{\varsigma}),\cdots,\eta_m(\boldsymbol{\varsigma})]^{\mathrm{T}}$, which is a function of the space coordinates of the IP $\bar{\mathbf{x}}$ (or $\bar{\boldsymbol{\varsigma}}$ in local coordinates).

For 2-D problems considered here, the basis functions are

$$\text{Linear}: \quad \boldsymbol{\psi}^{\mathrm{T}}(\boldsymbol{\varsigma}) = [1,\varsigma_1,\varsigma_2]\,, \tag{19}$$

$$\text{Quadratic (incomplete)}: \quad \boldsymbol{\psi}^{\mathrm{T}}(\boldsymbol{\varsigma}) = [1,\varsigma_1,\varsigma_2,\varsigma_1\varsigma_2]\,, \tag{20}$$

$$\text{Quadratic (complete)}: \quad \boldsymbol{\psi}^{\mathrm{T}}(\boldsymbol{\varsigma}) = \left[1,\varsigma_1,\varsigma_2,\varsigma_1^2,\varsigma_1\varsigma_2,\varsigma_2^2\right], \tag{21}$$

$$\text{Cubic (complete)}: \quad \boldsymbol{\psi}^{\mathrm{T}}(\boldsymbol{\varsigma}) = \left[1,\varsigma_1,\varsigma_2,\varsigma_1^2,\varsigma_1\varsigma_2,\varsigma_2^2,\varsigma_1^3,\varsigma_1^2\varsigma_2,\varsigma_1\varsigma_2^2,\varsigma_2^3\right]. \tag{22}$$

For a point $\boldsymbol{\varsigma}$ located on the fluid-solid interface, the normal gradient of $\varphi^h(\boldsymbol{\varsigma})$ can be expressed as

$$\frac{\partial}{\partial n}\varphi^h(\boldsymbol{\varsigma}) = \left[n_i\frac{\partial}{\partial\varsigma_i}\boldsymbol{\psi}^{\mathrm{T}}(\boldsymbol{\varsigma})\right]\boldsymbol{\eta}(\boldsymbol{\varsigma}) = \widehat{\boldsymbol{\psi}}^{\mathrm{T}}(\boldsymbol{\varsigma})\boldsymbol{\eta}(\boldsymbol{\varsigma}), \quad \forall\boldsymbol{\varsigma}\in\Gamma_{sf}\,, \tag{23}$$

in which

$$\widehat{\boldsymbol{\psi}}^{\mathrm{T}}(\boldsymbol{\varsigma}) = n_i\frac{\partial}{\partial\varsigma_i}\boldsymbol{\psi}^{\mathrm{T}}(\boldsymbol{\varsigma}), \tag{24}$$

and n_i is the direction cosine of $\mathbf{n}$ along the ς_i-axis.

The approximation of the value of φ at an IP $\bar{\mathbf{x}}$ is affected by the solution of the field equations in the fluid domain and boundary conditions on the fluid-solid interface. The relative importance of the field variables and the boundary conditions depends on the distance $d = |\bar{\mathbf{x}}-\mathbf{x}_{\mathrm{BI}}|$ between the IP and the BI $\mathbf{x}_{\mathrm{BI}}$. More specifically, the closer the IP is to the immersed boundary, the more dominant is the boundary condition on values at the IP. On the other hand, the farther the IP is from the immersed boundary, values of variables at the IP are influenced more by the solution of the field equations. Let N denote the number of nodes used to interpolate φ at the IP $\bar{\mathbf{x}}$. The value of N is determined by the number of nodes lying in the support domain Ω_l. In order that the local approximation is the best in a least-squares sense, the coefficient vector $\boldsymbol{\eta}(\boldsymbol{\varsigma})$ is selected by minimizing the following functional:

$$\mathcal{H}(\boldsymbol{\eta}) = \sum_{i=1}^{N}\mathcal{W}_i(\boldsymbol{\varsigma}-\boldsymbol{\varsigma}_i)\left[\boldsymbol{\psi}^{\mathrm{T}}(\boldsymbol{\varsigma})\boldsymbol{\eta}(\boldsymbol{\varsigma})-\varphi_i\right]^2, \tag{25}$$

subjected to the constraint

$$\widehat{\boldsymbol{\psi}}^{\mathrm{T}}(\boldsymbol{\varsigma})\boldsymbol{\eta}(\boldsymbol{\varsigma})-\mathcal{C} = 0. \tag{26}$$

In Equation 25, φ_i is the fictitious value of the variables at the fluid nodes $\mathbf{x}_i$ in the support domain Ω_l or at the BI $\mathbf{x}_{\mathrm{BI}}$, and $\mathcal{W}_i(\bar{\boldsymbol{\varsigma}}-\boldsymbol{\varsigma}_i)$ is the weight function associated with the positions of the IP and the fluid nodes. The constraint equation 26 represents the Neumann-type boundary conditions 17 and $\mathcal{C}$ is calculated from the right-hand side of Equation (17).

The problem of minimizing $\mathcal{H}(\boldsymbol{\eta})$ under the constraint expressed by Equation 26 is solved by using the penalty method. That is, the modified following functional

$$\widetilde{\mathcal{H}}(\boldsymbol{\eta}) = \sum_{i=1}^{N} \mathcal{W}_i(\boldsymbol{\varsigma}-\boldsymbol{\varsigma}_i)\left[\boldsymbol{\psi}^{\mathrm{T}}(\boldsymbol{\varsigma})\boldsymbol{\eta}(\boldsymbol{\varsigma})-\varphi_i\right]^2 + \kappa\left[\widehat{\boldsymbol{\psi}}^{\mathrm{T}}(\boldsymbol{\varsigma})\boldsymbol{\eta}(\boldsymbol{\varsigma})-\mathcal{C}\right]^2, \tag{27}$$

where κ is a preassigned penalty parameter, is minimized.

The stationary condition $\partial\widetilde{\mathcal{H}}/\,\partial\boldsymbol{\eta} = \mathbf{0}$ gives the following matrix equation

$$\mathscr{A}(\boldsymbol{\varsigma})\boldsymbol{\eta}(\boldsymbol{\varsigma}) = \mathscr{B}(\boldsymbol{\varsigma})\boldsymbol{\eta}(\boldsymbol{\varsigma}) + \mathbf{C}, \tag{28}$$

for the coefficient vector $\boldsymbol{\eta}(\boldsymbol{\varsigma})$. In Equation (28),

$$\mathscr{A}(\boldsymbol{\varsigma}) = \boldsymbol{\Psi}^{\mathrm{T}}\mathscr{W}\boldsymbol{\Psi} + \kappa\widehat{\boldsymbol{\psi}}^{\mathrm{T}}\widehat{\boldsymbol{\psi}}, \quad \mathscr{B}(\boldsymbol{\varsigma}) = \boldsymbol{\Psi}^{\mathrm{T}}\mathscr{W}\boldsymbol{\varphi}(\boldsymbol{\varsigma}), \quad \mathbf{C} = \kappa\widehat{\boldsymbol{\psi}}^{\mathrm{T}}(\mathbf{x})\mathcal{C}\,, \tag{29}$$

where

$$\boldsymbol{\Psi} = \begin{bmatrix} \psi_1(\boldsymbol{\varsigma}_1) & \psi_2(\boldsymbol{\varsigma}_1) & \cdots & \psi_m(\boldsymbol{\varsigma}_1) \\ \psi_1(\boldsymbol{\varsigma}_2) & \psi_2(\boldsymbol{\varsigma}_2) & \cdots & \psi_m(\boldsymbol{\varsigma}_2) \\ \cdots & \cdots & \cdots & \cdots \\ \psi_1(\boldsymbol{\varsigma}_N) & \psi_2(\boldsymbol{\varsigma}_N) & \cdots & \psi_m(\boldsymbol{\varsigma}_N) \end{bmatrix}, \quad \mathscr{W} = \begin{bmatrix} \mathcal{W}(\boldsymbol{\varsigma}-\boldsymbol{\varsigma}_1) & 0 & 0 & 0 \\ 0 & \mathcal{W}(\boldsymbol{\varsigma}-\boldsymbol{\varsigma}_2) & 0 & 0 \\ 0 & 0 & \ddots & 0 \\ 0 & 0 & 0 & \mathcal{W}(\boldsymbol{\varsigma}-\boldsymbol{\varsigma}_N) \end{bmatrix} \tag{30}$$

Substitution from Equation 28 for $\boldsymbol{\eta}(\boldsymbol{\varsigma})$ into Equation 18 leads to the following relation:

$$\varphi^h(\boldsymbol{\varsigma}) = \boldsymbol{\psi}^{\mathrm{T}}(\boldsymbol{\varsigma})\mathscr{A}^{-1}(\boldsymbol{\varsigma})\mathscr{B}(\boldsymbol{\varsigma})\boldsymbol{\varphi}(\boldsymbol{\varsigma}) + \boldsymbol{\psi}^{\mathrm{T}}(\boldsymbol{\varsigma})\mathscr{A}^{-1}(\boldsymbol{\varsigma})\mathbf{C}, \quad \forall\boldsymbol{\varsigma} \in \Omega_l\,, \tag{31}$$

Remark 1. *The constrained MLS approximation is well defined only when the matrix $\mathcal{A}(\boldsymbol{\varsigma})$ in Equation 28 is non-singular. This holds if the rank of the matrix $\boldsymbol{\Psi}$ equals m. A necessary condition for a well-defined approximation is that at least* m *weight functions are non-zero. The size of the local support domain Ω_l of any geometric shape should be large enough to cover a sufficient number of fluid nodes to ensure the regularity of the matrix $\mathcal{A}(\boldsymbol{\varsigma})$. In this work, the support of an image node $\overline{\boldsymbol{\varsigma}}$ is taken to be a circle of radius* $\mathrm{r_s}$ *centered at $\overline{\boldsymbol{\varsigma}}$. This allows for a high level of flexibility for choosing the fluid points. One needs to find a sufficient number of fluid points around the IP to accomplish the interpolation, and the simplest way is to increase the radius r_s until the required number of fluid interpolation points is identified.*

Remark 2. *The weight functions $\mathcal{W}_i(\boldsymbol{\varsigma}-\boldsymbol{\varsigma}_i)$ play an important role in the constrained MLS approximation. In practice, $\mathcal{W}_i(\boldsymbol{\varsigma}-\boldsymbol{\varsigma}_i)$ is generally chosen such that it is non-zero over the local support domain Ω_l. Here, the following power function is used as the weight function over Ω_l:*

$$\mathcal{W}_i(\boldsymbol{\varsigma}-\boldsymbol{\varsigma}_i) = \begin{cases} \left(1-r_i^2/r_s^2\right)^{\vartheta}, & \text{if } r_i \le r_s \\ 0, & \text{if } r_i > r_s \end{cases}, \tag{32}$$

where $r_i = |\varsigma_{\mathrm{i}} - \boldsymbol{\varsigma}|$ is the distance between the fluid node $\boldsymbol{\varsigma}_i$ and the point $\boldsymbol{\varsigma}$, and the integer ϑ can be adjusted to optimize the constrained MLS approximation. The variation of the weight function with the non-dimensional distance r_i/r_s for different values of ϑ is shown in Figure 2. It is observed that as the value of ϑ increases, the weighted influence in the constrained MLS approximation is significant for smaller values of r_i/r_s.

Remark 3. *To construct the normal velocity at an IP, the Dirichlet-type boundary condition needs to be enforced at the BI, i.e., $u_n = U_n$. In such a case, the penalty parameter κ in Equation 27 is taken as zero, and an unconstrained MLS approximation is used. For the interpolation of the mass density, the tangential velocity, and the pressure at an IP, 2 different situations are considered. If the IP is very close to the immersed boundary, then the constrained MLS scheme is used to construct these variables because the contributions of the Neumann-type boundary conditions of the immersed boundary are significant to the fluid values at the IP. However, when the IP is far away from the immersed boundary, then the Neumann-type boundary conditions are not considered in the MLS approximation of the variables at the IP. These 2 situations are monitored by checking the distance $|\boldsymbol{\varsigma}_{BI} - \boldsymbol{\varsigma}_{IP}|$*

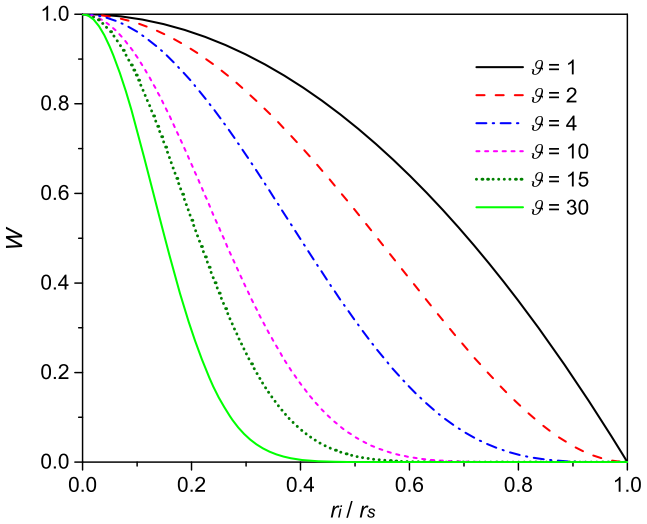

FIGURE 2 Variation with r_i/r_s of the weight function [Colour figure can be viewed at wileyonlinelibrary.com]

between the IP and the BI. If $|\bar{\xi}_{\mathrm{BI}}-\bar{\xi}_{\mathrm{IP}}|\leq \min\{\Delta x_1, \Delta x_2\}$, *the constrained MLS approximation is maintained; otherwise, the unconstrained MLS approximation is applied by setting* $\kappa=0$ *in Equation 27.*

Remark 4. *For a solid boundary with sharp corners or a slender body, the method of Chaudhuri et al*[23] *is used. The geometric data of the GPs are separately maintained for each space direction. The fluxes in the* x_1 and the x_2 directions are computed based on the GPs associated with the corresponding direction.

Once the flow variables at the IP have been computed, values of the flow variables at the corresponding GP are determined by using the boundary conditions on the immersed boundary. A linear interpolation along the normal is used and the value of the primitive variable at the GP is given by

$$\varphi_{\mathrm{GP}} = \mathcal{E}\varphi_{\mathrm{IP}} + \mathcal{Q}_{\mathrm{BI}}, \tag{33}$$

where φ_{GP} and φ_{IP} are flow variables at the GP and the IP, respectively; $\mathcal{Q}_{\mathrm{BI}}$ is evaluated at the BI; and $\mathcal{E}$ is a parameter. For Dirichlet-type boundary conditions (normal velocity), $\mathcal{Q}_{\mathrm{BI}} = 2\varphi_{\mathrm{BI}}$ and $\mathcal{E} = -1$; for Neumann-type boundary conditions (density, tangential velocity, and pressure), $\mathcal{E} = 1$ and $\mathcal{Q}_{\mathrm{BI}} = -\Delta l(\partial\varphi/\partial n)|_{\mathrm{BI}}$, where Δl is the distance between the ghost and the IPs. Note that Equation (33) results in a second-order accurate interpolation scheme.

Based on Equations 17 and 33, the flow variables at a GP are related to those of the IP by

$$\rho^{\mathrm{GP}} = \rho^{\mathrm{IP}}, \tag{34}$$

$$\boldsymbol{u}^{\mathrm{GP}} = \boldsymbol{u}^{\mathrm{IP}} - 2\left(\boldsymbol{u}^{\mathrm{IP}}\cdot\boldsymbol{n}\right)\boldsymbol{n} + 2\left(\boldsymbol{U}^{\mathrm{BI}}\cdot\boldsymbol{n}\right)\boldsymbol{n}, \tag{35}$$

$$E^{\mathrm{GP}} = \frac{p^{\mathrm{GP}}}{\gamma-1} + \frac{1}{2}\rho^{\mathrm{GP}}\left|\boldsymbol{u}^{\mathrm{GP}}\right|^2, \tag{36}$$

in which

$$p^{\mathrm{GP}} = p^{\mathrm{IP}} - \Delta l\left(\frac{\rho u_\tau^2}{R} - \rho\frac{D\boldsymbol{u}}{Dt}\cdot\boldsymbol{n}\right)\Bigg|_{\mathrm{BI}}. \tag{37}$$

The previous equations complete the numerical evaluation of values of the flow variables at the GPs.

The boundary treatment outlined is for non-moving solid bodies provided that the grid-interface relation, and the flow variables at the GPs are updated at each time step. However, the role of a fixed Cartesian grid node near the immersed interface may vary as the solid body moves across a node. As shown in Figure 3, an interior fluid node at time t_{n-1} may become a newly

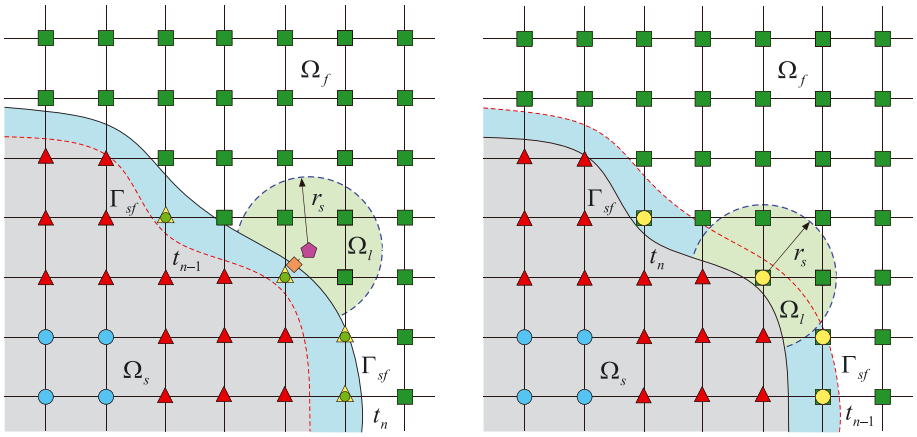

FIGURE 3 Immersed interface moving relative to the Cartesian grid. Left, boundary intrudes into the fluid (△ newly emerging GP); right, boundary withdraws from the fluid (○ newly emerging FP) [Colour figure can be viewed at wileyonlinelibrary.com]

emerged GP at time t_n as the boundary intrudes on to the fluid region, or a GP at t_{n-1} may become a newly emerged fluid node (called "fresh point", i.e., FP) at t_n as the boundary withdraws from the fluid region. For the first case, the solution for the fluid can be advanced in time since all flow variables in the fluid region at time t_n are well defined. The computation of values at each newly emerged GP follows the same procedure as that for a normal GP. Complications are encountered in the second case because the newly emerged FPs were previously in the solid and they have no history in the fluid phase at current time t_n. To close the equations, the flow variables at the FPs are determined by a field-extension procedure.[24] A normal intercept is extended from a FP to the boundary and this intersects at a BI. Because the simulations of the fluid flow are limited by the Courant-Friedrich-Levy (CFL) condition, the moving velocities of the immersed boundary are also subject to a similar constraint. This implies that, for any time step, the distance between a FP and a BI is less than the minimum grid spacing, i.e., $|\varsigma_{BI} - \varsigma_{FP}| < \min\{\Delta x_1, \Delta x_2\}$. The values of flow variables at each FP are interpolated by using the constrained MLS method, and the interpolation procedure for the FP is similar to that of an IP.

3.3 | Loosely coupled partitioned algorithm

Equations for the fluid and the solid are solved by a loosely coupled and serially staggered algorithm. The solution procedure for the entire domain is summarized below:

- The position of the rigid solid and the mass density, the velocity, and the pressure of the fluid are known at time t_n.
- The fluid pressure exerted on the rigid solid is determined. Knowing the total force and the total torque applied on the solid, the position of the solid is advanced to time t_{n+1} by solving Equations 4 and 5 with the implicit Newmark integration scheme.
- The position, the velocity, and the acceleration of the solid are updated. Image points and GPs at time t_{n+1} are determined by the ray-tracing method. The flow variables at the GPs are determined using the sharp interface immersed boundary method. The density, the velocity and the pressure of the fluid are then computed at time t_{n+1}.
- Proceed to the next time step.

4 | RESULTS AND DISCUSSION

In order to demonstrate the accuracy and the robustness of the proposed method, 5 problems of varying complexity involving compressible flows over stationary and moving solids have been solved. These FSIs encompass a number of flow phenomena, including shock reflection, diffraction, etc. The accuracy of the method is discussed by comparing present results with the previously published analytical and computational ones. The CFL number that must be less than 1 for stability of the numerical solution is set equal to 0.3 for all problems studied herein.

Unless otherwise mentioned, the incomplete polynomials defined in Equation 20 are adopted in the MLS interpolation. Suitably non-dimensionalized values of variables are used, the penalty parameter κ in the constrained MLS method is taken $=10^3$, and in the radius $r_s = \beta\sqrt{(\Delta x_1)^2 + (\Delta x_2)^2}$ of the support domain, we set $\beta = 3.0$.

4.1 | Double Mach reflection of a strong shock

The first problem analyzed is usually known as the double Mach reflection test,[25] which is commonly used to evaluate the performance of high resolution schemes. This problem is described by a right-moving shock wave, initially perpendicular to the x direction and encountering an inclined rigid wedge. As vividly discussed by Woodward and Colella,[25] a number of shock-wave reflection phenomena (e.g., regular, single, complex, and double Mach reflection) may appear depending on the Mach number of the incident shock wave and the angle of the wedge. The computational domain for this problem is taken as $[0, 2] \times [0, 1]$, and the rigid wedge starts from $x = 1/6$ making 30° angle with the bottom surface. An initial right-moving planar shock wave of Mach number 10 is set at $x = 1/6$. The pre-shock values of the mass density and the pressure are: $\rho = 1.4$ and $p = 0$, and their post-shock values are found by using the Rankine-Hugoniot conditions. The fluid is assumed to slip on the wedge surface, and on all other boundaries, the Dirichlet-type conditions are used. The contours of the computed density at $t = 0.09$ using a 800×400 uniform grid are given in Figure 4.

It is observed from Figure 4 that a complex shock structure with 2 triple points evolves when the shock runs up the wedge. The incident shock, the reflected shock, and the Mach stem come across at the primary triple point; a bow-shaped shock, a Mach stem, and a secondary reflected shock form the secondary triple point. Slip lines emanate from the 2 triple points. A curled flow structure is generated when the reflected shock hits the primary slip line, and its resolution measures the robustness of the numerical scheme. The main challenge in applying a high-resolution scheme to this problem is the delineation of the secondary slip lines.[25] As shown in Figure 4, all of the above-mentioned flow structures are well captured by the present method. We refer to Woodward and Colella[25] and Chi et al[26] for similar results obtained with a grid-aligned method.

The computed results for the mass density along the wedge surface are shown in Figure 5 for simulations performed using 400×200, 500×250, 600×300, and 800×400 uniform grids. The presently computed results are compared with the

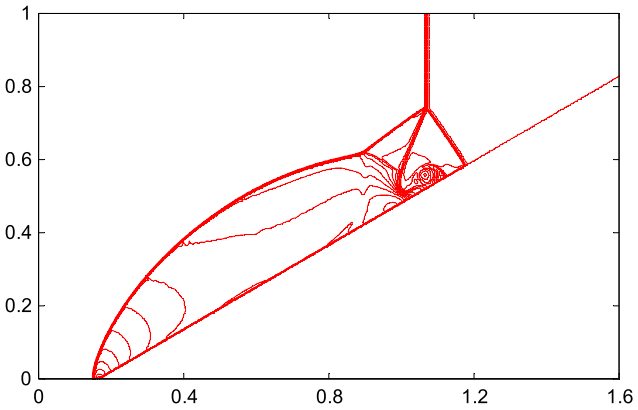

FIGURE 4 Contours of the mass density at $t = 0.09$(60 contours plotted within the density range [0, 21.82]) [Colour figure can be viewed at wileyonlinelibrary.com]

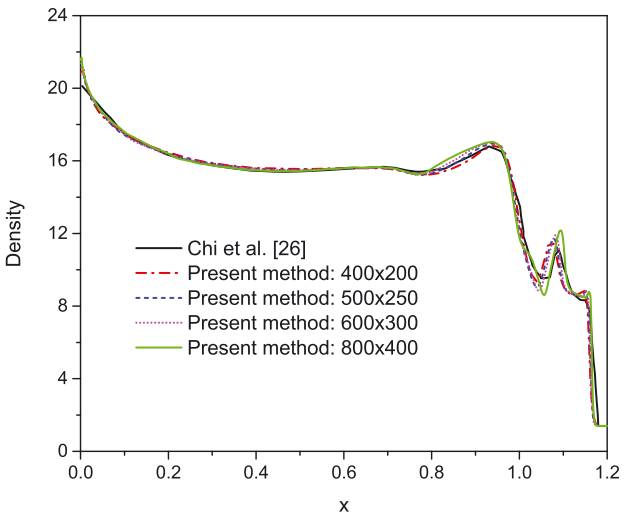

FIGURE 5 Comparison of the variation of the mass density along the wedge surface [Colour figure can be viewed at wileyonlinelibrary.com]

grid-aligned solutions of Chi et al[26] who used a rotational transformation technique and assumed that the shock wave moves at an angle of 60° to the x_1-axis and the domain boundary at the bottom is reflective from $x = 1/6$. This configuration does not require dealing with the cut-cell problem of the wedge surface and can be used as a reference for comparison. As shown in Figure 5, the present results converge very fast except in the region of the curled flow. The results obtained with a coarse grid 400×200 are in satisfactory agreement with the reference solutions.

To illustrate the effect of the penalty parameter on the numerical solutions, we have plotted in Figure 6 the mass density along the wedge surface by using the 800×400 uniform grid and different values of the penalty parameter. Note that for the unconstrained MLS method, $\kappa = 0$. It is found that negative values of the mass density and of the pressure occur for $\kappa = 0$, and numerical results do not converge. However, the constrained MLS method is stable for a large range of values of κ, i.e., $10 \leq \kappa \leq 10^8$, and provides converged solutions. It is not required that κ be large enough for the boundary conditions to be well satisfied, and $\kappa = 10^3$ always gave converged results.

Figure 7 shows the effect of the support domain size on the accuracy of the mass density and the pressure on the wedge surface. The density and the pressure are evaluated at each solid marker on the wedge surface, and the support domain of a solid marker $\hat{\boldsymbol{\varsigma}}$ is taken as a circle of radius $r_s = \beta\sqrt{(\Delta x_1)^2 + (\Delta x_2)^2}$ centered at $\hat{\boldsymbol{\varsigma}}$. The simulations are performed on a 800×400 uniform grid. In order to show the performance of the constrained MLS method, the inversed distance weighted (IDW) interpolation scheme[7,11,12] commonly used in the immersed boundary methods is also used to evaluate the mass density and the pressure at each solid marker on the wedge surface. The same Dirichlet- and Neumann- boundary conditions used in the constrained MLS method are considered in the IDW interpolation scheme. From Figure 7, it is observed that for the constrained MLS method, reasonably accurate solutions of the mass density and the pressure are obtained by using support domains with

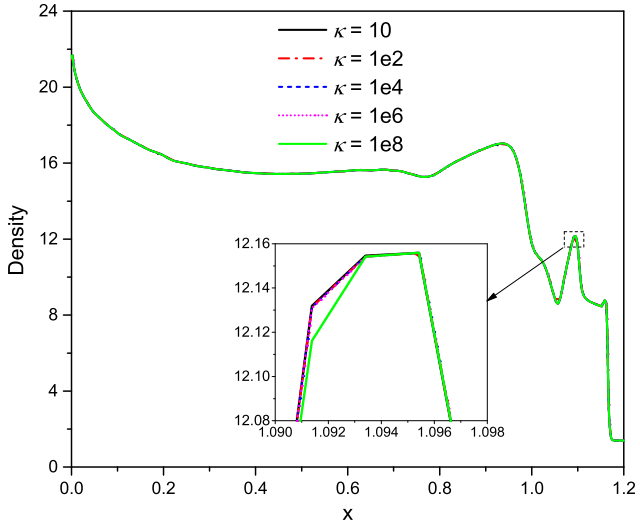

FIGURE 6 For $10 \leq \kappa \leq 10^8$ variation of the computed mass density along the wedge surface [Colour figure can be viewed at wileyonlinelibrary.com]

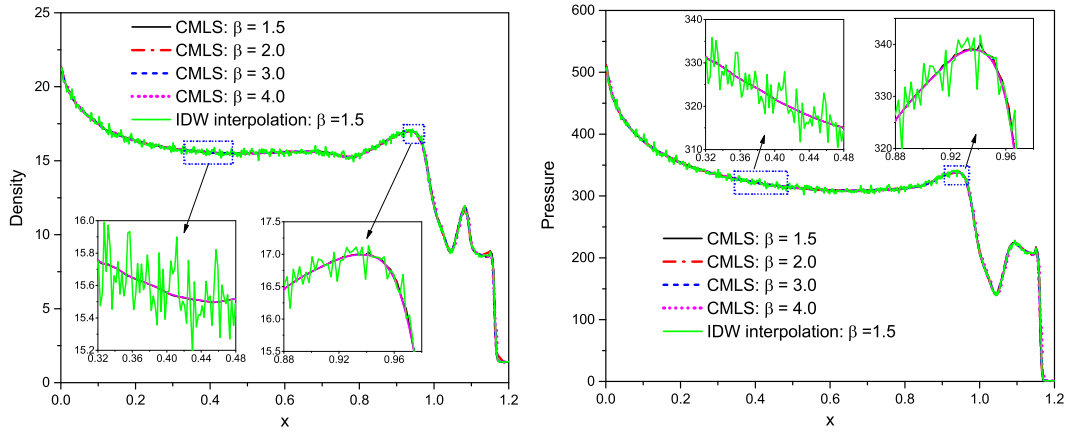

FIGURE 7 Effects of the support domain radius on the mass density and the pressure distributions along the wedge surface. Left, density distribution; right, pressure distribution [Colour figure can be viewed at wileyonlinelibrary.com]

small radii. An increase in the radius of the support domain does not significantly affect the mass density and the pressure distributions on the wedge surface. As mentioned previously, the number of fluid points in a support domain of small radius may not be sufficient for a well-posed problem in the unconstrained MLS method. However, in the constrained MLS method, the flow variables on the solid surface are mostly affected by the boundary conditions, and the penalty term plays an important role in the constrained MLS formulation, which always leads to a well-posed least-squares interpolation. This implies that in the constrained MLS method, a support domain with a small radius can be used to interpolate the flow variables near the immersed boundary. Therefore, the present method can potentially work for computing flows with small gaps without using local grid refinement. In addition, the results in Figure 7 show that the IDW interpolation scheme leads to oscillations in the density and pressure distributions. However, changing the support domain radius in the IDW interpolation scheme cannot eliminate the oscillations in the results.

4.2 | Mach 3 flow in a wind tunnel with a forward facing step

We consider a 2-D wind tunnel flow past a rigid step that has been extensively studied (e.g., see Refs. 27,28). Figure 8 shows the geometry and the boundary conditions. All boundary conditions except those for the inflow, the outflow, and the rigid step are imposed by reflecting boundaries. The fluid is allowed to slip on the surface of the step. The outflow boundary is calculated by interpolating states of interior nodes. The problem is initialized by a right-going Mach 3 flow.

The computed density contours at $t=2.0$ and $t=4.0$ by using a 600×300 uniform grid, $r_s = 2.5\sqrt{(\Delta x_1)^2 + (\Delta x_2)^2}$ and $\kappa = 1 \times 10^3$, are given in Figure 9. Although a singularity exists at the corner of the step, no special technique near the corner is used. It is clear that the method effectively captures all features of the flow field, and the density contours compare very closely with those obtained by Smith et al.[27]

4.3 | Supersonic flow over a circular bump

This problem is studied to demonstrate the application of the constrained MLS method for a compressible flow of the inflow Mach number 1.65 past a solid with a curved boundary. The dimensions of the channel and the circular bump are depicted in Figure 10. The slip conditions are applied on the upper and the lower surfaces of the channel. Because flow at the outlet is supersonic, all variables at the right boundary of the channel are extrapolated.

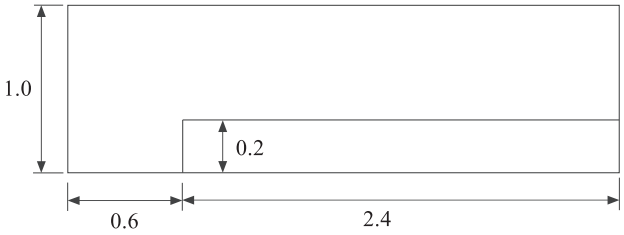

FIGURE 8 Geometry of a Mach 3 wind tunnel with a forward facing step

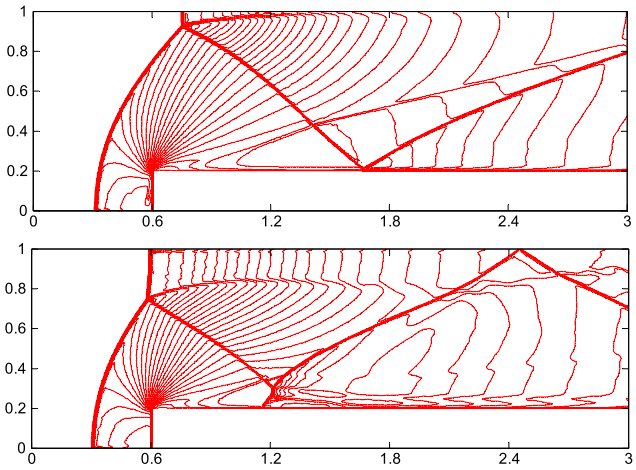

FIGURE 9 Forward step problem. Top, $t=2.0$ (30 equally spaced density contours from 0.19 to 6.99); bottom, $t=4.0$ (30 equally spaced density contours from 0.32 to 6.15) [Colour figure can be viewed at wileyonlinelibrary.com]

Contours of the computed Mach number using a 600×200 uniform grid are shown in Figure 11. It is observed that 2 oblique shocks are generated at the 2 corners of the bump, and the leading edge shock reflected from the top wall intersects with the shock leaving the trailing edge. The reflection and the intersection of the shocks are very well resolved without introducing oscillations. This is in excellent agreement with the results of Ref. 29.

The computed Mach number profiles along the lower and the upper walls of the channel are depicted in Figure 12. These converged solutions obtained with 600×200 and 900×300 grids are compared with those of Moukalled and Darwish[29] using the body-fitted method. It is evident that the present solutions using the 600×200 grid are in good agreement with those of Ref. 29.

A grid resolution study is performed to analyze the convergence rate or the accuracy of the constrained MLS method. The computed L_2 and L_∞ error norms of the density are shown in Figure 13. The L_2 error norm is a good measure of the global error, and the L_∞ error norm effectively captures the local error around the immersed boundary. Because exact solutions do not exist for this problem, the numerical solution obtained with the 1200×400 uniform grid is used as a baseline for computing errors. A line denoting the second-order convergence rate is also included in the log-log plot. Although the incomplete polynomials defined in Equation 20 are used in the constrained MLS interpolation, the results show that the proposed constrained MLS immersed boundary method is globally and locally second-order accurate for the flow interacting with a stationary rigid body.

4.4 | Moving piston in 2-D shock tube

For flows involving moving boundaries, a problem involving a rigid piston translating at a constant velocity in a 2-D shock tube is examined. The dimensions of the shock tube are $L \times H = 1\text{m} \times 0.2\,\text{m}$; the location and the geometric data of the piston

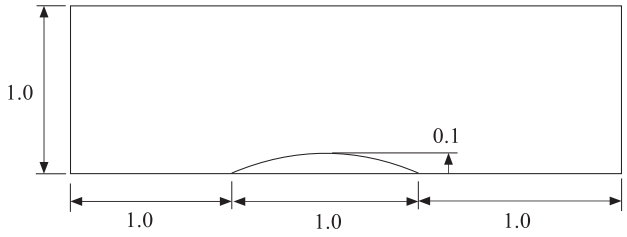

FIGURE 10 Compressible flow past a circular bump

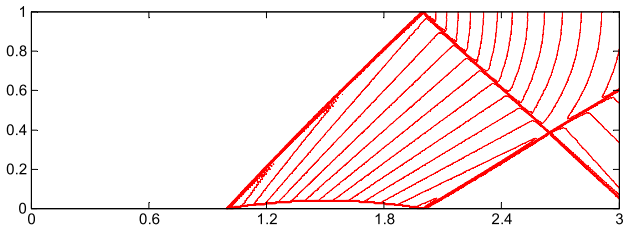

FIGURE 11 Contours of the Mach number for a supersonic flow over a bump [Colour figure can be viewed at wileyonlinelibrary.com]

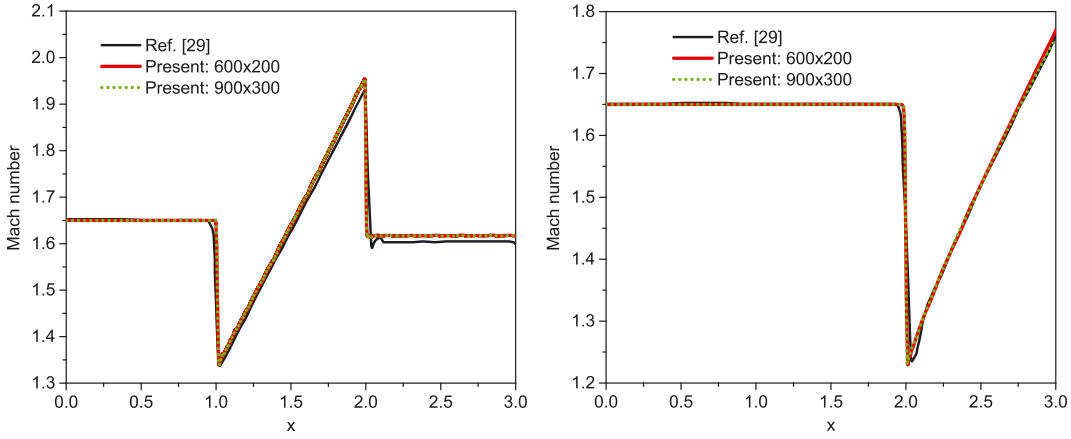

FIGURE 12 Variation along the channel length of the Mach number at the upper (right) and the lower (left) boundaries of the channel [Colour figure can be viewed at wileyonlinelibrary.com]

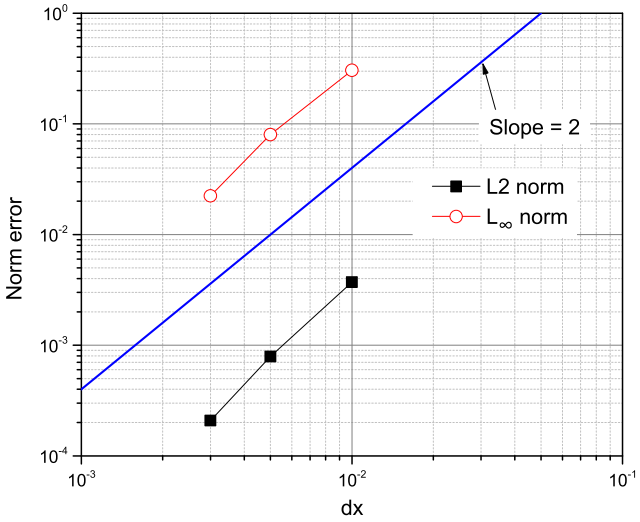

FIGURE 13 L_2 and L_∞ norms of the error in the density versus the computational grid size [Colour figure can be viewed at wileyonlinelibrary.com]

are $(X, Y) = [0.4\text{ m}, 0.44\text{ m}] \times [0\text{ m}, 0.2\text{ m}]$. The piston instantaneously moves from left to right with a constant speed $u = 300$ m/s into an initially quiescent fluid with $\rho = 1.0$ kg/m^3 and $p = 10^5$ Pa. In Figure 14, we have exhibited, for 4 values of the penalty parameter κ, the computed profiles of the mass density and the velocity using the 400×60 uniform grid. The mass density and the axial velocity distributions along the x-axis on the line $y = 0.1$ m at time $t = 8 \times 10^{-4}$ s are compared with the exact solutions given by Shyue.[30] It is observed that for $\kappa = 0$, spurious density with a large value appears behind the piston, and the velocity oscillates at the location of the rarefaction wave head. It is because the flow variables at the fresh nodes cannot be accurately reconstructed by the unconstrained MLS method. However, for $\kappa \geq 10$, results obtained by the constrained MLS method seem unchanged and agree well with the exact solutions.

In order to find how coarse a grid one can use to get good results, we used 3 different grids, 200×40, 600×80, and 800×160. The density and the axial velocity at time $t = 8 \times 10^{-4}$ s along the line $y = 0.1$ m depicted in Figure 15 reveal that numerical results obtained even with a relatively coarse 200×40 grid are in excellent agreement with the exact solutions, and the present approach predicts the correct shock location. The $x - t$ diagrams of the density and the pressure are shown in Figure 16.

The computed L_2 and L_∞ error norms of the mass density are plotted in Figure 17 versus the grid size. A line representing the second-order accuracy slope is also included. It is clear that for a moving boundary problem, the proposed constrained MLS immersed boundary method is globally and locally second-order accurate.

4.5 | Lift-off problem of a rigid circular cylinder

The moving body problem studied by Monasse et al[31] and Pasquariello et al[32] is now simulated. The setup consists of a 2-D channel filled with air and a rigid cylinder of density 7.6 kg/m^3 and a diameter of 0.1 m, initially resting on the lower wall

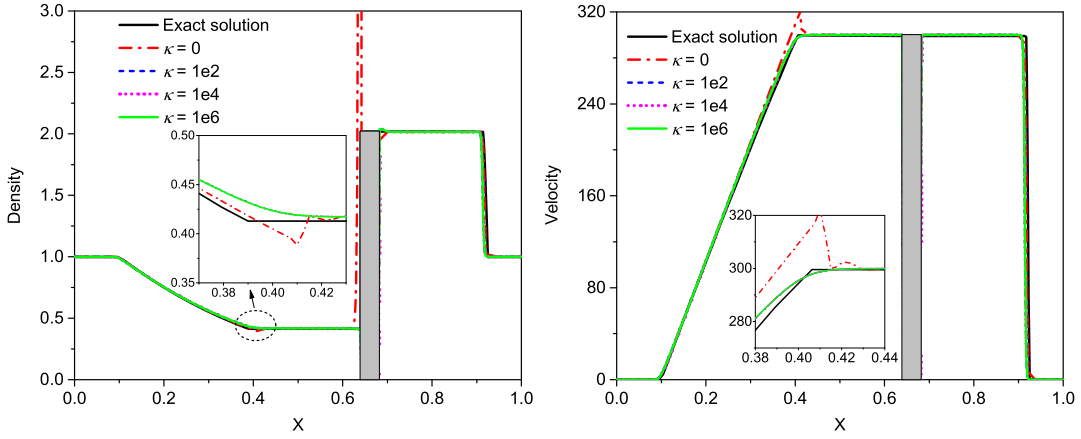

FIGURE 14 Comparison of the computed density and velocity profiles with the exact solutions [Colour figure can be viewed at wileyonlinelibrary.com]

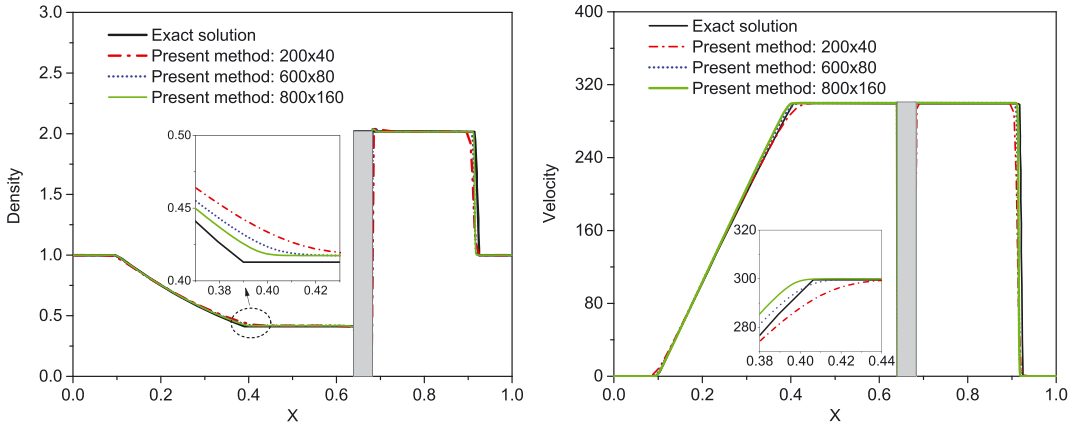

FIGURE 15 For 3 uniform grids, variation of the computed mass density and the axial velocity [Colour figure can be viewed at wileyonlinelibrary.com]

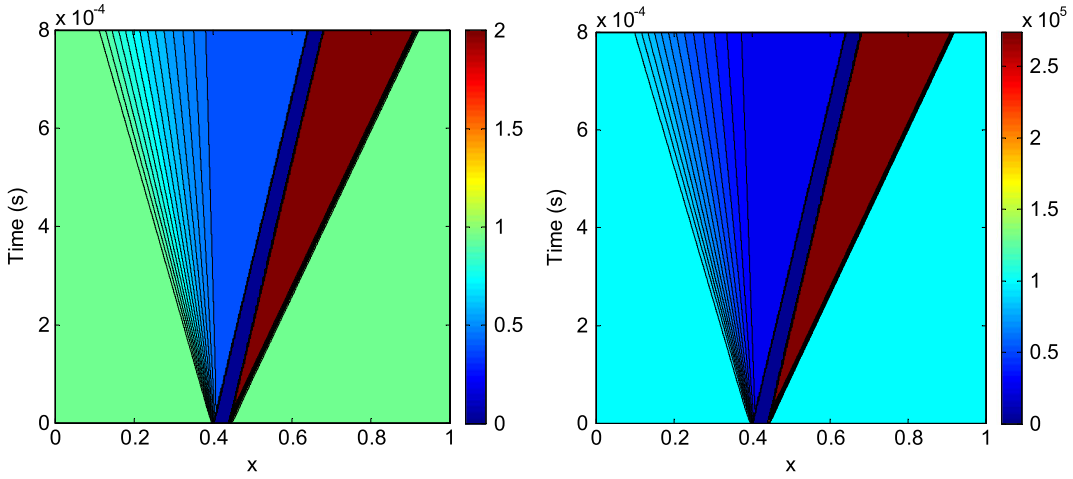

FIGURE 16 The $x-t$ diagrams of the mass density and the pressure (the position of the solid is in shown dark blue color). Left, density; right, pressure

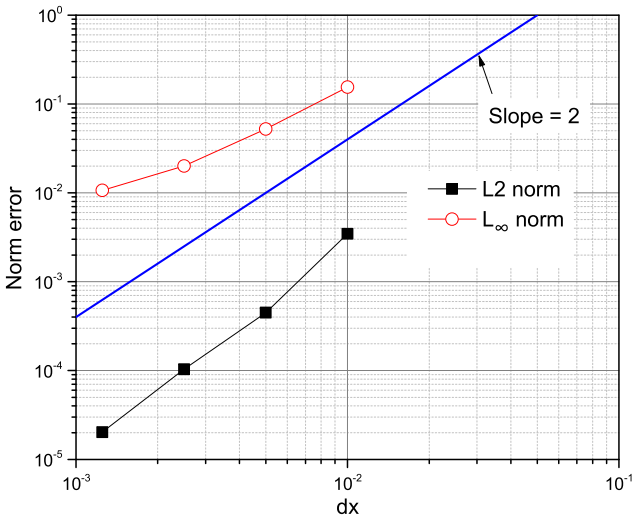

FIGURE 17 L_2 and L_∞ norms of the error in the density versus the computational grid size [Colour figure can be viewed at wileyonlinelibrary.com]

at the position: $(X_c, Y_c) = (0.15\text{ m}, 0.05\text{ m})$. The cylinder is driven and lifted upwards by an incident shock wave with $M_a = 3$ starting at $x = 0.08$ m. The pre-shock conditions are prescribed as $\rho = 1$ kg/m^3, $u = v = 0$ m/s, and $p = 1$ Pa for $x \geq 0.08$, and the post-shock conditions for $x < 0.08$ as $\rho = 3.857$ kg/m^3, $u = 2.629$ m/s, $v = 0$ m/s, and $p = 10.33$ Pa. The rectangular fluid

domain has dimensions 1.0 m × 0.2 m. The boundary conditions on the left surface are set as inflow with the corresponding post-shock flow parameters. The right-side boundary conditions are non-reflecting, while slipping of the fluid is allowed on the top and the bottom rigid walls.

The computed results for the horizontal and the vertical positions of the mass center of the cylinder at $t = 0.255$ s are compared in Figure 18 with those of Monasse et al[31] and Pasquariello et al.[32] Different grid resolutions of $1/dx = 1/dy = 400$, 600, and 800 are used in the computation. The presently computed final position of the cylinder is in reasonable agreement with those of the 2 reference solutions.

The instantaneous density and pressure contours computed using a uniform 800 × 160 grid at $t = 0.14$ s and 0.255 s are presented in Figures 19 and 20, respectively. The results show that the solid positions and the shock patterns determined by the present method agree well with those reported by Monasse et al[31] and Pasquariello et al.[32] A strong vortex below the rigid cylinder exists throughout the entire cylinder trajectory, which is also reported by Monasse et al[31] and Pasquariello et al.[32] This vortex is probably associated with a Kelvin-Helmholtz instability of the contact discontinuity present under the cylinder.

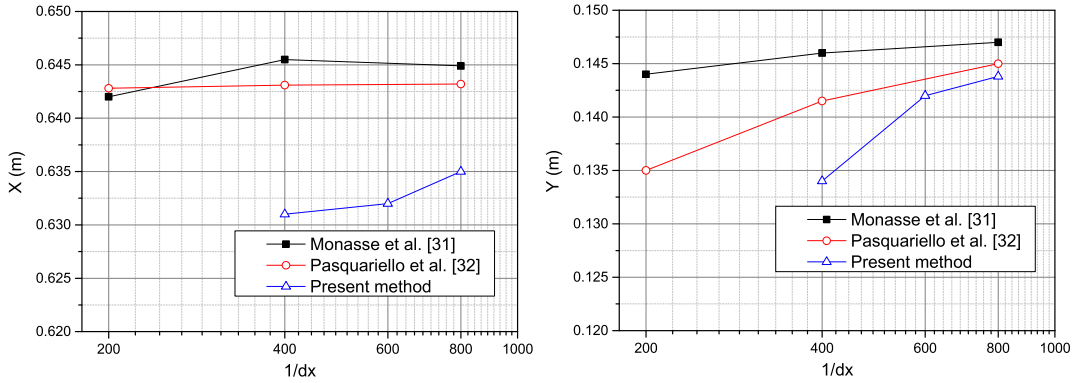

FIGURE 18 Computed results for the cylinder center position for 3 grids in the fluid domain: horizontal position (left), vertical position (right) [Colour figure can be viewed at wileyonlinelibrary.com]

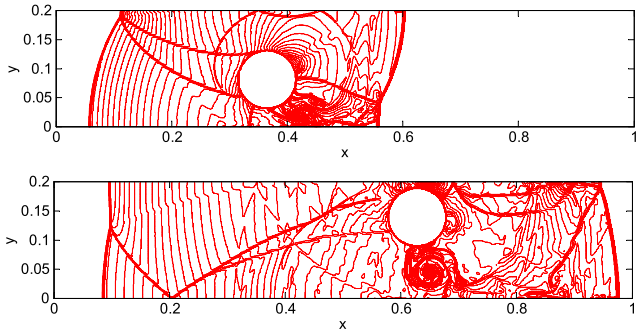

FIGURE 19 Density contours at 2 different times: (top) $t = 0.140$ s (50 contours from 0 to 7.8); (bottom) $t = 0.255$ s (50 contours from 0 to 6) [Colour figure can be viewed at wileyonlinelibrary.com]

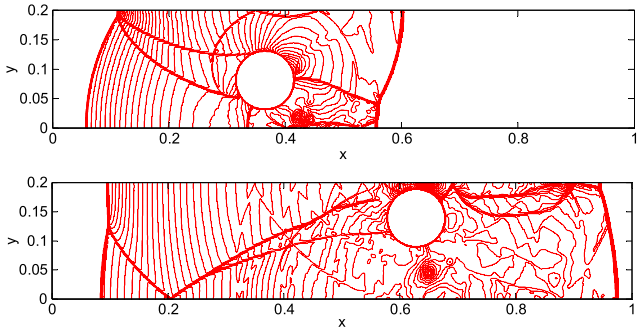

FIGURE 20 Pressure contours at 2 different times: (top) $t = 0.140$ s (50 contours from 0 to 28); (bottom) $t = 0.255$ s (50 contours from 0 to 22) [Colour figure can be viewed at wileyonlinelibrary.com]

5 | CONCLUSIONS

A ghost-cell sharp interface method combined with a constrained MLS approximation is developed to implement boundary conditions on the fluid-solid interface for compressible flows over irregularly shaped either stationary or moving rigid solids. The fluid flow equations are discretized by the Lax-Friedrichs flux splitting scheme, and the spatial derivatives are approximated by using the finite difference method based on the fifth-order weighted essentially non-oscillatory scheme. The interpolation of the flow variables at an image node is implemented by a constrained moving least-squares interpolation method. The Dirichlet- and the Neumann-type boundary conditions on the fluid-solid interface are enforced in the interpolation process. The computed results for the following 5 challenging problems have been found to compare well with those available in the literature: (i) double Mach reflection of a strong shock, (ii) Mach 3 flow in a wind tunnel with a forward facing step, (iii) supersonic flow over a circular bump, (iv) moving piston in a 2-D shock tube, and (v) lift-off problem of a rigid circular cylinder. It validates the accuracy of the present method in analyzing the fluid-rigid solid interaction problems.

We note that instead of using a penalty parameter in Equation (27), one could use the method of Lagrange multipliers to enforce the constraint expressed by Equation (26), e.g., see Refs. 33 and 34.

ACKNOWLEDGMENTS

RCB's work was partially supported by the US Office of Naval Research grant no. N00014-16-1-2309 to Virginia Polytechnic Institute and State University with Dr. Y.D.S. Rajapakse as the program manager. Views expressed in the paper are those of the authors and not of the ONR.

REFERENCES

1. Donea J, Giuliani S, Halleux J. An arbitrary Lagrangian–Eulerian finite element method for transient dynamic fluid–structure interactions. *Comput Methods Appl Mech Eng*. 1982;33:689-723.
2. Slone AK, Pericleous K, Bailey C, Cross M. Dynamic fluid–structure interaction using finite volume unstructured mesh procedures. *Comput Struct*. 2002;80:371-390.
3. Sotiropoulos F, Yang X. Immersed boundary methods for simulating fluid–structure interaction. *Progress in Aerospace Sciences*. 2014;65:1-21.
4. Peskin CS. Flow patterns around heart valves: a numerical method. *J Comput Phys*. 1972;10:252-271.
5. Goldstein D, Handler R, Sirovich L. Modeling a no-slip flow boundary with an external force field. *J Comput Phys*. 1993;105:354-366.
6. Lai MC, Peskin CS. An immersed boundary method with formal second-order accuracy and reduced numerical viscosity. *J Comput Phys*. 2000;160:705-719.
7. Tseng Y-H, Ferziger JH. A ghost-cell immersed boundary method for flow in complex geometry. *J Comput Phys*. 2003;192:593-623.
8. Udaykumar HS, Mittal R, Rampunggoon P, Khanna A. A sharp interface Cartesian grid method for simulating flows with complex moving boundaries. *J Comput Phys*. 2001;174:345-380.
9. Mittal R, Dong H, Bozkurttas M, Najjar FM, Vargas A, von Loebbecke A. A versatile sharp interface immersed boundary method for incompressible flows with complex boundaries. *J Comput Phys*. 2008;227:4825-4852.
10. Ghias R, Mittal R, Dong H. A sharp interface immersed boundary method for compressible viscous flows. *J Comput Phys*. 2007;225:528-553.
11. Gilmanov A, Sotiropoulos F, Balaras E. A general reconstruction algorithm for simulating flows with complex 3D immersed boundaries on Cartesian grids. *J Comput Phys*. 2003;191:660-669.
12. Gao T, Tseng Y-H, Lu X-Y. An improved hybrid Cartesian/immersed boundary method for fluid–solid flows. *Int J Numer Methods Fluids*. 2007;55:1189-1211.
13. Peller N, Duc AL, Tremblay F, Manhart M. High-order stable interpolations for immersed boundary methods. *Int. J. Numer. Methods Fluids*. 2006;52:1175-1193.
14. Vanella M, Balara E. A moving-least-squares reconstruction for embedded-boundary formulations. *J Comput Phys*. 2009;228:6617-6628.
15. Seo JH, Mittal R. A high-order immersed boundary method for acoustic wave scattering and low-Mach number flow-induced sound in complex geometries. *J Comput Phys*. 2011;230:1000-1019.
16. Toro EF. *Riemann solvers and numerical methods for fluid dynamics: a practical introduction*. 3rd ed. Berlin: Springer-Verlag; 2009:129-133.
17. Liu XD, Osher S, Chan T. Weighted essentially non-oscillatory schemes. *J Comput Phys*. 1994;115:202-212.
18. Balsara DS, Shu CW. Monotonicity preserving weighted essentially non-oscillatory schemes with increasingly high order of accuracy. *J Comput Phys*. 2000;160:405-452.

19. Borges R, Carmona M, Costa B, Don WS. An improved weighted essentially nonoscillatory scheme for hyperbolic conservation laws. *J Comput Phys*. 2008;227:3101-3211.
20. Nonomura T, Morizawa S, Terashima H, Obayashi S, Fujii K. Numerical (error) issues on compressible multicomponent flows using a high-order differencing scheme: Weighted compact nonlinear scheme. *J Comput Phys*. 2012;231:3181-3210.
21. O'Rourke J. *Computational Geometry in C*. Cambridge, UK: Cambridge University Press; 1998.
22. Sambasivan SK, UdayKumar HS. Ghost fluid method for strong shock interactions part 2: Immersed solid boundaries. *AIAA Journal*. 2009;47:2923-2937.
23. Chaudhuri A, Hadjadj A, Chinnayya A. On the use of immersed boundary methods for shock/obstacle interactions. *J Comput Phys*. 2011;230:1731-1748.
24. Yang J, Balaras E. An embedded-boundary formulation for large-eddy simulation of turbulent flows interacting with moving boundaries. *J Comput Phys*. 2006;215:12-40.
25. Woodward P, Colella P. The numerical simulation of two-dimensional fluid flow with strong shocks. *J Comput Phys*. 1984;54:115-173.
26. Chi C, Lee BJ, Im HG. An improved ghost-cell immersed boundary method for compressible flow simulations. *Int J Numer Methods Fluids*. 2016. https://doi.org/10.1002/fld.4262
27. Smith MR, Cave HM, Wu JS, Jermy MC, Chen Y-S. An improved quiet direct simulation method for Eulerian fluids using a second-order scheme. *J Comput Phys*. 2009;228:2213-2224.
28. Zhu J, Zhong X, Shu CW, Qiu J. Runge–Kutta discontinuous Galerkin method using a new type of WENO limiters on unstructured meshes. *J Comput Phys*. 2013;248:200-220.
29. Moukalled F, Darwish M. A high-resolution pressure-based algorithm for fluid flow at all speeds. *J Comput Phys*. 2001;168:101-130.
30. Shyue K-M. *A Moving-Boundary Tracking Algorithm for Inviscid Compressible Flow, Hyperbolic Problems: Theory, Numerics, Applications*. Berlin Heidelberg: Springer; 2008:989-996.
31. Monasse L, Daru V, Mariotti C, Piperno S, Tenaud C. A conservative coupling algorithm between a compressible flow and a rigid body using an embedded boundary method. *J Comput Phys*. 2012;231:2977-2994.
32. Pasquariello V, Hammerl G, Örley F, et al. A cut-cell finite volume–finite element coupling approach for fluid–structure interaction in compressible flow. *J Comput Phys*. 2016;307:670-695.
33. Batra RC, Porfiri M, Spinello D. Treatment of material discontinuity in two meshless local Petrov-galerkin (MLPG) formulations of axisymmetric transient heat conduction. *Int J Numer Methods Eng*. 2004;61:2461-2479.
34. Batra RC, Porfiri M, Spinello D. Analysis of electrostatic MEMS using meshless local petrov-galerkin method. *Eng Anal Boundary Elem*. 2006;30:949-962.

How to cite this article: Qu Y, Batra RC. Constrained moving least-squares immersed boundary method for fluid-structure interaction analysis. *Int J Numer Meth Fluids*. 2017;85:675–692. https://doi.org/10.1002/fld.4400